RESEARCH ARTICLE

Spatially inhomogeneous non-Hermitian topological metasurfaces

Jie Chang[1], Xianghong Kong[2,3], Yuhsuan Lai[4], Bohan Jiang[1], Xiaoxing Yin[1], Zhixia Xu[1,*]

[1]State Key Laboratory of Millimeter Waves, Southeast University, Nanjing 210096, China

[2]Department of Electrical and Computer Engineering, National University of Singapore, Singapore 117583, Singapore

[3]National University of Singapore Suzhou Research Institute, Suzhou 215123, China

[4]School of Architecture, Southeast University, Nanjing 210096, China

Corresponding author. E-mail: *zhixiaxu@seu.edu.cn

Received April 3, 2026; accepted July 15, 2026

Supporting Information

Contents

S1. Band Structure of Hermitian and Non-Hermitian Topological Lattice

To further clarify the physical distinction between the Hermitian and non-Hermitian inhomogeneous systems, we quantitatively analyze how the engineered loss reshapes the complex band structure near the Γ point. Figure S1(a) shows the unit cell of the microstrip topological lattice. The Hermitian counterpart is obtained by replacing the resistive elements with lossless metallic connections, while the non-Hermitian model retains the loaded resistors.

Figures S1(b) and S1(c) compare the calculated band structures of the Hermitian and non-Hermitian unit cells. In the Hermitian case, all eigenfrequencies are purely real, and the degeneracy is a conventional real-frequency degeneracy. In the non-Hermitian case, the eigenfrequencies become complex. The real parts of the bands form a finite degenerate line near the Γ point, while the imaginary parts exhibit a clear bifurcation, indicating that the degenerate branches possess different attenuation rates.

To quantify this non-Hermitian spectral reconstruction, we define L_{dege} as the normalized wave-vector length of the real-part degenerate region near the Γ point, where the frequency separation between the two branches satisfies $|\Delta\mathrm{Re}(f)| < 0.1$ GHz. We further define $\Delta\mathrm{Im}(f)$ as the maximum splitting of the imaginary eigenfrequency between the two branches along this real-part degenerate region. Figures S1(d) and S1(e) show the extracted L_{dege} and $\Delta\mathrm{Im}(f)$ as functions of the loaded resistance. Both quantities increase within the investigated resistance range, demonstrating that the real-part degenerate line and the associated imaginary spectral bifurcation are tunable non-Hermitian effects. This behavior is absent in the Hermitian limit, where $\mathrm{Im}(f) = 0$ and no loss-induced bifurcation exists.

Figure S2 compares the band diagrams and field distributions of the Hermitian and non-Hermitian unit cells along the high-symmetry path. In the lossless case, the unit cell exhibits fourfold degeneracy at the Γ point. Symmetry breaking opens a bandgap at this Γ point. When losses are included, the real-frequency gap is suppressed near the Γ point, and the corresponding modes form a real-part degenerate region accompanied by imaginary-frequency bifurcation. The corresponding field profiles also change significantly due to the resistive elements.

Figure S3 shows the tight-binding (TB) model corresponding to the electromagnetic structure and its band diagram. The TB results agree well with the eigenmode results. The Hamiltonian of the TB model is expressed as

$$H(k)=\begin{pmatrix} im_a & t_a & 0 & t_b e^{i\left(-k_x/2+\sqrt{3}k_y/2\right)} & 0 & t_a \\ t_a & im_b & t_a & 0 & t_b e^{-ik_x} & 0 \\ 0 & t_a & im_a & t_a & 0 & t_b e^{i\left(-k_x/2-\sqrt{3}k_y/2\right)} \\ t_b e^{i\left(-k_x/2+\sqrt{3}k_y/2\right)} & 0 & t_a & im_b & t_a & 0 \\ 0 & t_b e^{-ik_x} & 0 & t_a & im_a & t_a \\ t_a & 0 & t_b e^{i\left(-k_x/2-\sqrt{3}k_y/2\right)} & 0 & t_a & im_b \end{pmatrix} \tag{S1}$$

where k_x and k_y are the wave vectors, t_a and t_b denote intra- and intercell coupling strengths, and im_a, im_b represent non-Hermitian onsite terms. To correspond with the electromagnetic model in Fig. 1, we set $t_a = 1$, $t_b = 1.5$, $m_a = 0$, and $m_b = -2$.

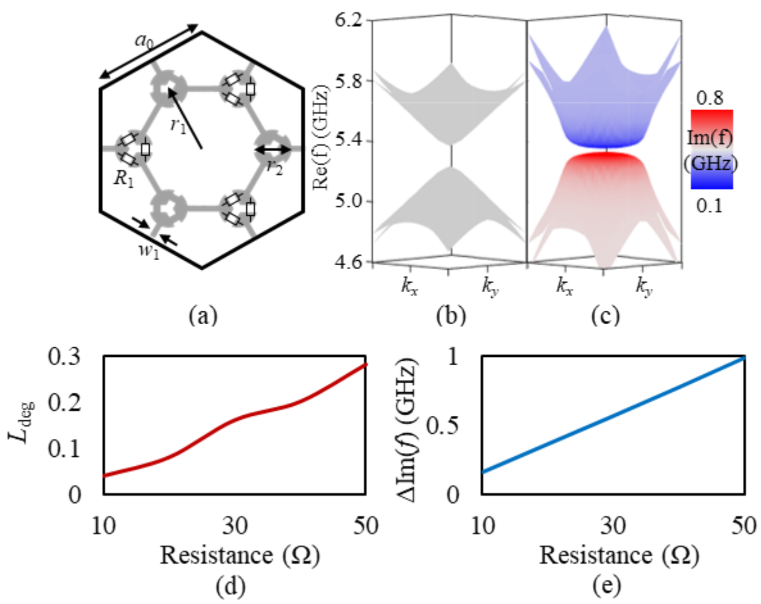

Fig. S1 Hermitian/non-Hermitian comparison and resistance-dependent complex-spectral bifurcation. (a) Unit cell of the microstrip topological lattice with resistive loading. The Hermitian counterpart is obtained by replacing the resistors with lossless metallic connections while keeping the same geometry. (b) Band structure of the Hermitian unit cell, where all eigenfrequencies are real and the degeneracy corresponds to a conventional real-frequency degeneracy. (c) Complex band structure of the non-Hermitian unit cell. The color map denotes the imaginary part of the eigenfrequency, showing that the real-part degenerate region is accompanied by a clear imaginary-frequency bifurcation. (d) Extracted normalized length (L_{dege}) of the real-part degenerate region as a function of the loaded resistance. (e) Maximum imaginary-frequency splitting $\Delta\mathrm{Im}(f)$ along the real-part degenerate region as a function of the loaded resistance. The vanishing of $\Delta\mathrm{Im}(f)$ in the Hermitian limit confirms that the spectral bifurcation is induced by the engineered non-Hermitian dissipation.

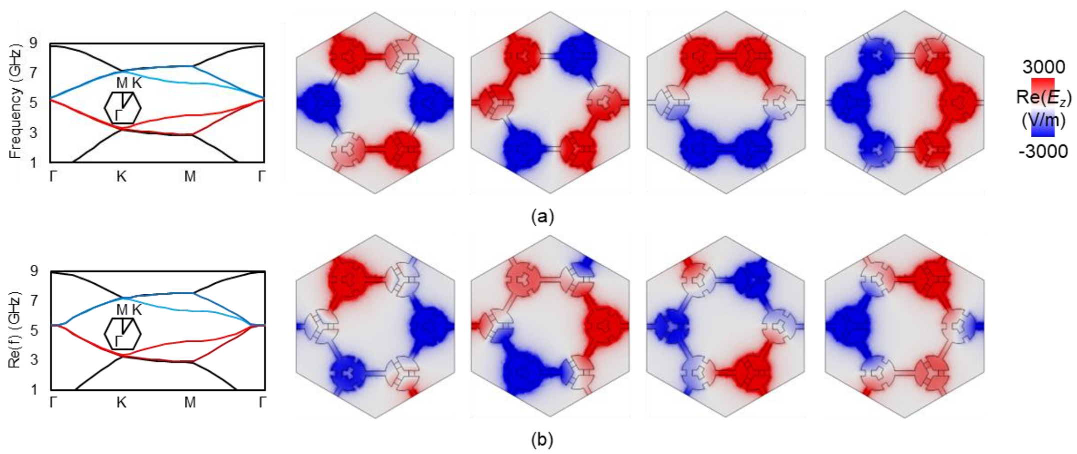

Fig. S2 (a) Band structure and eigenmode field distribution of the Hermitian unit cell. (b) Band structure and eigenmode field distribution of the non-Hermitian unit cell.

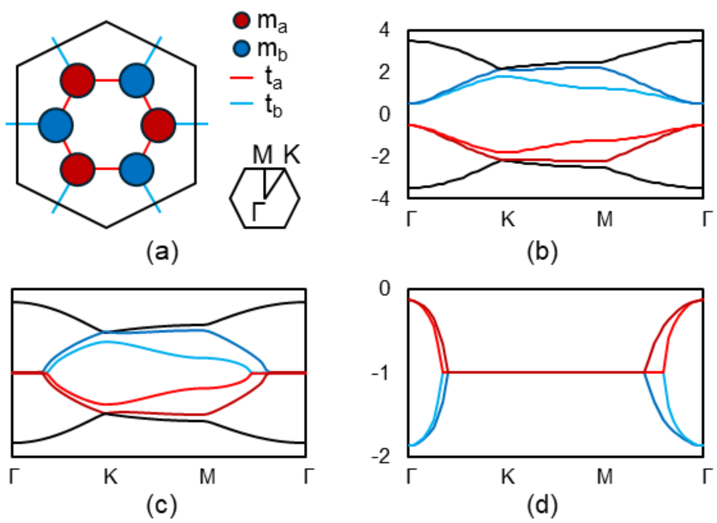

Fig. S3 (a) Theoretical tight-binding model. (b) Band structure of the Hermitian TB model. (c) Real part of the non-Hermitian band frequency. (d) Imaginary part of the non-Hermitian band frequency.

S2. Wilson-loop calculation of the tight-binding model

To verify the topological character of the bulk bands, we calculated the Wilson-loop spectrum of the six-site tight-binding model. In the calculations shown in Fig. S4, we compare the Hermitian case ($m_a = 0$, $m_b = 0$) with a representative lossy case ($m_a = 0$, $m_b = -0.5$).

Because the first three bands constitute a connected band subspace, the Wilson loop was calculated using the non-Abelian overlap matrix rather than treating the bands independently. For a set of N_b bands, the overlap matrix between two neighboring momentum points k_j and k_{j+1} is defined as

$$S_{mn}(\mathbf{k}_j,\mathbf{k}_{j+1}) = \left\langle u_m\left(\mathbf{k}_j\right)\middle| u_n\left(\mathbf{k}_{j+1}\right)\right\rangle, \qquad m,n=1,\ldots,N_b \tag{S2}$$

Here, $u_n(\mathbf{k})$ is the periodic part of the Bloch eigenstate of the n-th band. In the present calculation, N_b=3, corresponding to the first three bands. Equivalently, the overlap matrix $S(\mathbf{k}_j,\ \mathbf{k}_{j+1})$ can be written as

$$S\left(\mathbf{k}_j,\mathbf{k}_{j+1}\right)=\begin{bmatrix} \left\langle u_1\left(\mathbf{k}_j\right)\middle|u_1\left(\mathbf{k}_{j+1}\right)\right\rangle & \left\langle u_1\left(\mathbf{k}_j\right)\middle|u_2\left(\mathbf{k}_{j+1}\right)\right\rangle & \cdots & \left\langle u_1\left(\mathbf{k}_j\right)\middle|u_{N_b}\left(\mathbf{k}_{j+1}\right)\right\rangle \\ \left\langle u_2\left(\mathbf{k}_j\right)\middle|u_1\left(\mathbf{k}_{j+1}\right)\right\rangle & \left\langle u_2\left(\mathbf{k}_j\right)\middle|u_2\left(\mathbf{k}_{j+1}\right)\right\rangle & \cdots & \left\langle u_2\left(\mathbf{k}_j\right)\middle|u_{N_b}\left(\mathbf{k}_{j+1}\right)\right\rangle \\ \vdots & \vdots & \ddots & \vdots \\ \left\langle u_{N_b}\left(\mathbf{k}_j\right)\middle|u_1\left(\mathbf{k}_{j+1}\right)\right\rangle & \left\langle u_{N_b}\left(\mathbf{k}_j\right)\middle|u_2\left(\mathbf{k}_{j+1}\right)\right\rangle & \cdots & \left\langle u_{N_b}\left(\mathbf{k}_j\right)\middle|u_{N_b}\left(\mathbf{k}_{j+1}\right)\right\rangle \end{bmatrix} \tag{S3}$$

The Wilson matrix along a closed loop in momentum space is then obtained as

$$W\left(\mathbf{k}_{\parallel}\right)=\prod_{\mathrm{j}=1}^{N_k} S\left(\mathbf{k}_j,\mathbf{k}_{j+1}\right) \tag{S4}$$

Here, $\mathbf{k}_{\parallel}$ labels the transverse momentum of the Wilson loop, and N_k is the number of discretized points along the closed loop. The Wilson-loop phases are extracted from the eigenvalues of $W(\mathrm{k}_{\parallel})$,

$$\theta_n\left(\mathbf{k}_{\parallel}\right)=-\mathrm{Im}\left[\ln\lambda_n\left(W\left(\mathbf{k}_{\parallel}\right)\right)\right], \qquad n=1,\ldots,N_b \tag{S5}$$

where $\lambda_n(W)$ is the n-th eigenvalue of the Wilson matrix. For the non-Hermitian case, the Hamiltonian satisfies $H \neq H^{\dagger}$, and the right eigenvectors are generally not orthogonal under the conventional inner product. Therefore, we used the biorthogonal form of the overlap matrix,

$$S_{mn}^{LR}\left(\mathbf{k}_j,\mathbf{k}_{j+1}\right)=\left\langle u_m^L\left(\mathbf{k}_j\right)\middle|u_n^R\left(\mathbf{k}_{j+1}\right)\right\rangle, \qquad m,n=1,\ldots,N_b \tag{S6}$$

In matrix form,

$$S^{LR}\left(\mathbf{k}_j,\mathbf{k}_{j+1}\right)=\begin{bmatrix} \left\langle u_1^L\left(\mathbf{k}_j\right)\middle|u_1^R\left(\mathbf{k}_{j+1}\right)\right\rangle & \left\langle u_1^L\left(\mathbf{k}_j\right)\middle|u_2^R\left(\mathbf{k}_{j+1}\right)\right\rangle & \cdots & \left\langle u_1^L\left(\mathbf{k}_j\right)\middle|u_{N_b}^R\left(\mathbf{k}_{j+1}\right)\right\rangle \\ \left\langle u_2^L\left(\mathbf{k}_j\right)\middle|u_1^R\left(\mathbf{k}_{j+1}\right)\right\rangle & \left\langle u_2^L\left(\mathbf{k}_j\right)\middle|u_2^R\left(\mathbf{k}_{j+1}\right)\right\rangle & \cdots & \left\langle u_2^L\left(\mathbf{k}_j\right)\middle|u_{N_b}^R\left(\mathbf{k}_{j+1}\right)\right\rangle \\ \vdots & \vdots & \ddots & \vdots \\ \left\langle u_{N_b}^L\left(\mathbf{k}_j\right)\middle|u_1^R\left(\mathbf{k}_{j+1}\right)\right\rangle & \left\langle u_{N_b}^L\left(\mathbf{k}_j\right)\middle|u_2^R\left(\mathbf{k}_{j+1}\right)\right\rangle & \cdots & \left\langle u_{N_b}^L\left(\mathbf{k}_j\right)\middle|u_{N_b}^R\left(\mathbf{k}_{j+1}\right)\right\rangle \end{bmatrix} \tag{S7}$$

The right and left eigenvectors satisfy,

$$H(\mathbf{k})\left|u_n^R(\mathbf{k})\right\rangle = E_n(\mathbf{k})\left|u_n^R(\mathbf{k})\right\rangle, \tag{S8a}$$

$$H^{\dagger}(\mathbf{k})\left|u_n^L(\mathbf{k})\right\rangle = E_n^{*}(\mathbf{k})\left|u_n^L(\mathbf{k})\right\rangle, \tag{S8b}$$

and are normalized according to the biorthogonal condition

$$\left\langle u_m^L(\mathbf{k})\middle|u_n^R(\mathbf{k})\right\rangle=\delta_{mn} \tag{S9}$$

The non-Hermitian Wilson matrix is then calculated by replacing $S(\mathbf{k}_j,\ \mathbf{k}_{j+1})$ in Eq. (S4) with $S^{LR}(\mathbf{k}_j,\ \mathbf{k}_{j+1})$. The Wilson-loop eigenphases are gauge invariant when the overlap matrix and boundary gauge are defined consistently. In this work, we adopt the biorthogonal left-right form because it naturally accounts for the non-orthogonality of the right eigenvectors in the non-Hermitian system.

Figure S4 shows the real band structures and the corresponding Wilson-loop spectra. In the Hermitian limit, the Wilson-loop spectrum exhibits the characteristic nontrivial behavior of the topological lattice. Under moderate non-Hermitian loss, the real band structure remains continuously connected to the Hermitian case, and the Wilson-loop spectrum retains the same qualitative feature. This confirms that the non-Hermitian lossy system is topologically connected to the Hermitian phase as long as the selected three-band subspace remains separated from the upper bands.

For stronger loss, the complex spectral separation between the selected three-band subspace and the remaining bands can become small. In that regime, the Wilson-loop spectrum may be distorted and should not be used alone to define an independent band-subspace topological invariant. Therefore, in this work, the Wilson-loop calculation is used to establish the adiabatic connection between the Hermitian topological phase and the weak-to-moderate non-Hermitian lossy regime.

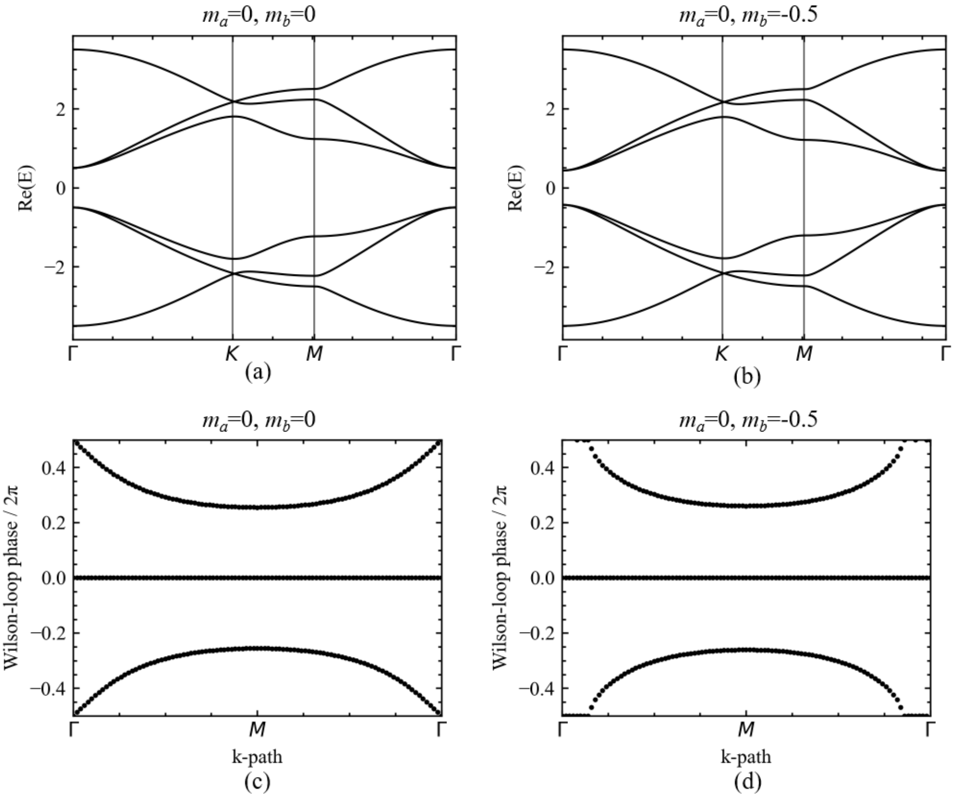

Fig. S4 Real band structures and Wilson-loop spectra of the tight-binding model. (a,b) Real parts of the bulk bands for ($m_a = 0$, $m_b = 0$) and ($m_a = 0$, $m_b = -0.5$), respectively. Here, $m_b = -0.5$ corresponds to an onsite loss term $im_b = -0.5i$. (c,d) Corresponding Wilson-loop spectra calculated for the first three-band subspace. The persistence of the Wilson-loop structure under moderate loss indicates that the non-Hermitian system is topologically connected to the Hermitian limit.

S3. Bulk Bands Extracted from the Full-Wave Model via 2D FFT

Figure S5(a) shows a photograph of the fabricated microstrip sample used for bulk-band measurements. A linearly polarized source was placed at the center of the sample, and a probe scanned the electric-field distribution. By performing a 2D fast Fourier transform (FFT) of the measured field, the 3D bulk band structure shown in Fig. S5(b) was obtained.

Figure S6 illustrates the band-extraction process of the simulated full model for comparison with experiment. Figures S6(a) and (b) show the real- and reciprocal-space representations of the unit cell. Since the microstrip supports a dominant quasi-TEM mode, only the fundamental mode contributes to the measured band. Thus, the 2D-FFT-derived band does not exhibit the automatic folding seen in the eigenmode solver. The correct band structure is reconstructed by sampling along the folded path in reciprocal space. Figures S6(c), S6(d), and S6(e) present the simulated 3D bulk band, contour plots of eigenfrequencies, and the band structure along the high-symmetry path, respectively.

Figure S7 shows the corresponding results for the Hermitian structure. A 2D FFT of the simulated electric field yields the 3D band diagram in Fig. S7(a). Due to the C_{6v} symmetry, the unit cell acts as a higher-order perturbation element, leading to band folding and fourfold degeneracy. In experiments, the unfolded bands are observed. Figure S7(b) gives the equal-frequency contours at representative frequencies, and Fig. S7(c) shows the corresponding band diagram.

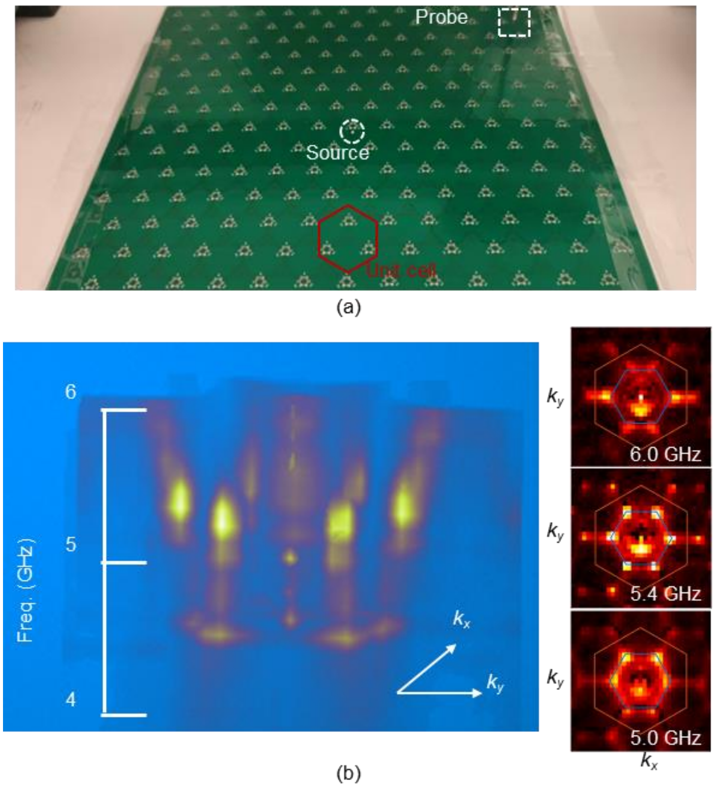

Fig. S5 (a) Photograph of the fabricated microstrip topological lattice. (b) Extracted 3D bulk band and eigenfrequency contours at discrete frequencies.

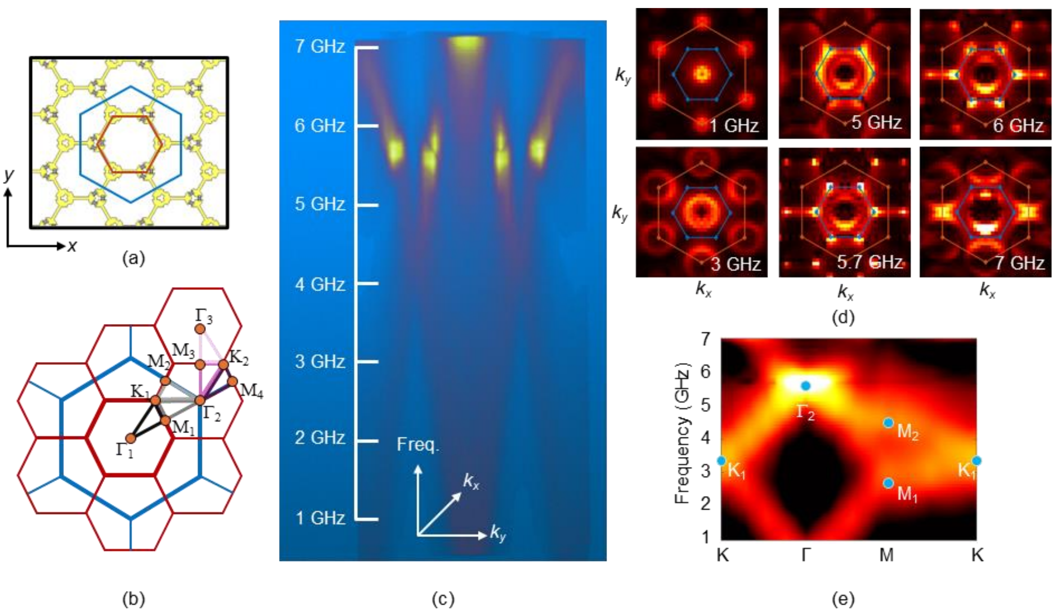

Fig. S6 (a) Photograph of the microstrip topological metasurface decorated with resistors. (b) Schematic of the high-symmetry path after band folding. (c) Simulated 3D bulk band of the non-Hermitian model. (d) Eigenfrequency contours at six discrete frequencies. (e) Band diagram along the high-symmetry path.

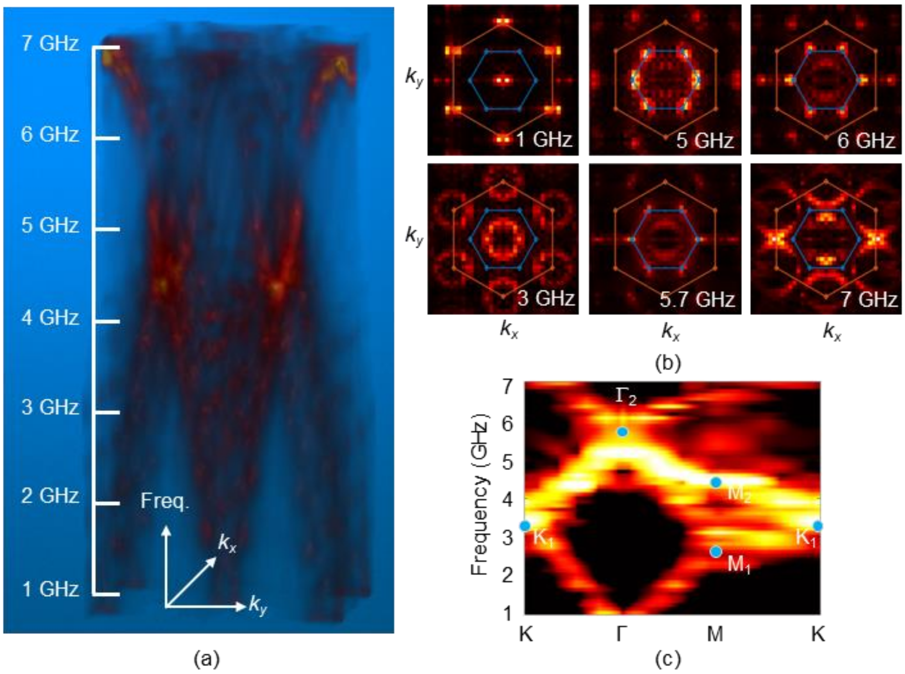

Fig. S7 (a) 3D bulk bands extracted from full-wave simulations of the Hermitian model. (b) Eigenfrequency contours at six discrete frequencies. (c) Band diagram along the high-symmetry path.

S4. Eigenmode Analysis of Edge States in the Inhomogeneous Lattice

Figure S8 shows the dispersion and field profiles of the Hermitian inhomogeneous lattice. When resistive loading is introduced, the eigenfrequencies become complex and the edge dispersion develops a real-part degenerate segment accompanied by imaginary-frequency splitting. Figure S9 shows the six-resistor configuration, where the real-frequency gap between the two edge branches is suppressed. Figure S10 presents the real and imaginary components of the corresponding tight-binding dispersion, consistent with the electromagnetic results.

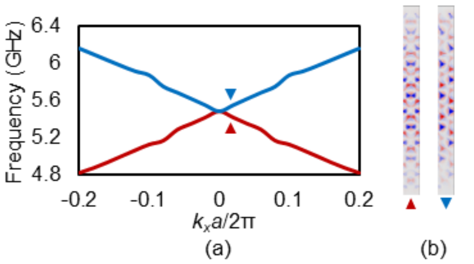

Fig. S8 (a) Dispersion of the Hermitian inhomogeneous lattice. (b) Eigenmode field distribution.

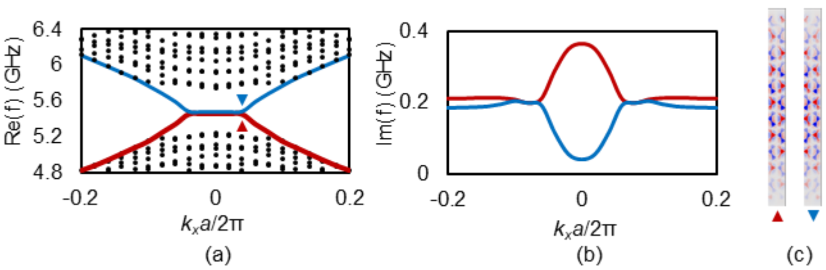

Fig. S9 (a) Real part of the non-Hermitian band for the six-resistor case. (b) Imaginary part of the non-Hermitian band. (c) Eigenmode field distribution.

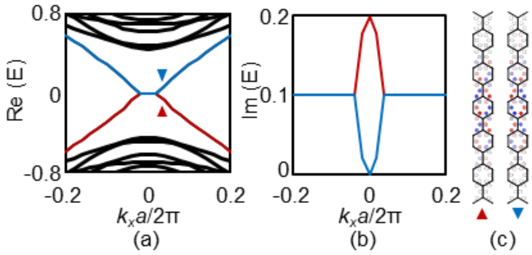

Fig. S10 (a) Real part of the tight-binding band. (b) Imaginary part of the tight-binding band. (c) Field distributions.

S5. Clarification of the Mass-Gradient Domain-Wall Mechanism

Spatially inhomogeneous lattices can lead to different effective continuum descriptions depending on how the structural modulation enters the Dirac Hamiltonian. When the modulation changes the kinetic coupling terms, it may act as an artificial vector potential and generate a pseudo-magnetic field, leading to Landau-level-like quantization. This mechanism is distinct from the one used in the present metasurface.

In our design, the continuous transition from shrunken to expanded unit cells primarily modulates the Dirac mass term m(y). The resulting effective Hamiltonian is therefore described as a mass-gradient domain-wall system rather than an artificial-gauge-field-induced Landau-level system. The sign change and spatial variation of m(y) determine the local bandgap evolution and confine the interface modes near the domain wall.

The effect of the geometric gradient is quantified by the transverse field profiles and the extracted localization length. As shown in Fig. S11 and Fig. S12, increasing the gradient step size Δr steepens the spatial variation of the mass term and reduces the localization length of the edge modes. This confirms that the geometric inhomogeneity controls the confinement of the domain-wall interface modes. The additional non-Hermitian physics arises from the resistive loading, which reshapes the spectrum in the complex-frequency plane and produces the imaginary-frequency bifurcation discussed in Fig. S1.

S6. Quantitative Localization Analysis of the Adiabatic Edge States

In our spatially inhomogeneous metasurface, the topological domain wall is created by a continuous geometric gradient rather than a sharp discrete boundary. According to the physics of adiabatic topological interfaces, such smooth spatial transitions inherently allow the edge states to penetrate deeper into the surrounding lattice, resulting in a broader transverse field profile compared to conventional hard-wall topological insulators.

To quantitatively confirm the topological confinement of these adiabatic edge states and evaluate the impact of the gradient step size Δr, we extracted the 1D transverse electric field profiles $|E_{avg}|$ across the supercell (Figure S11(a)) and calculated the effective localization length L_{loc} using the standard Inverse Participation Ratio (IPR) method. The localization length is defined as:

$$L_{loc} = \left[\frac{\int |E_{avg}|^4 \, dx}{\left(\int |E_{avg}|^2 \, dx \right)^2} \right]^{-1} \tag{S10}$$

where the integration is performed along the transverse y-axis.

Figure S11 displays the electric field envelopes for the two non-Hermitian edge modes (Mode 1 and Mode 2) at the degenerate center under varying geometric gradient step sizes (Δr = 0.1, 0.2, and 0.3 mm). The extracted localization lengths are plotted in Figure S12. The data reveal a clear monotonic trend: as the gradient step size Δr increases, the spatial variation of the effective Dirac mass term becomes steeper. Consequently, both non-Hermitian edge modes are subjected to stronger topological confinement, causing their localization lengths to decrease monotonically. This quantitative contraction confirms that the observed modes are interface-localized topological edge states bounded to the domain wall, rather than extended bulk modes, and their confinement can be effectively tuned by the structural gradient.

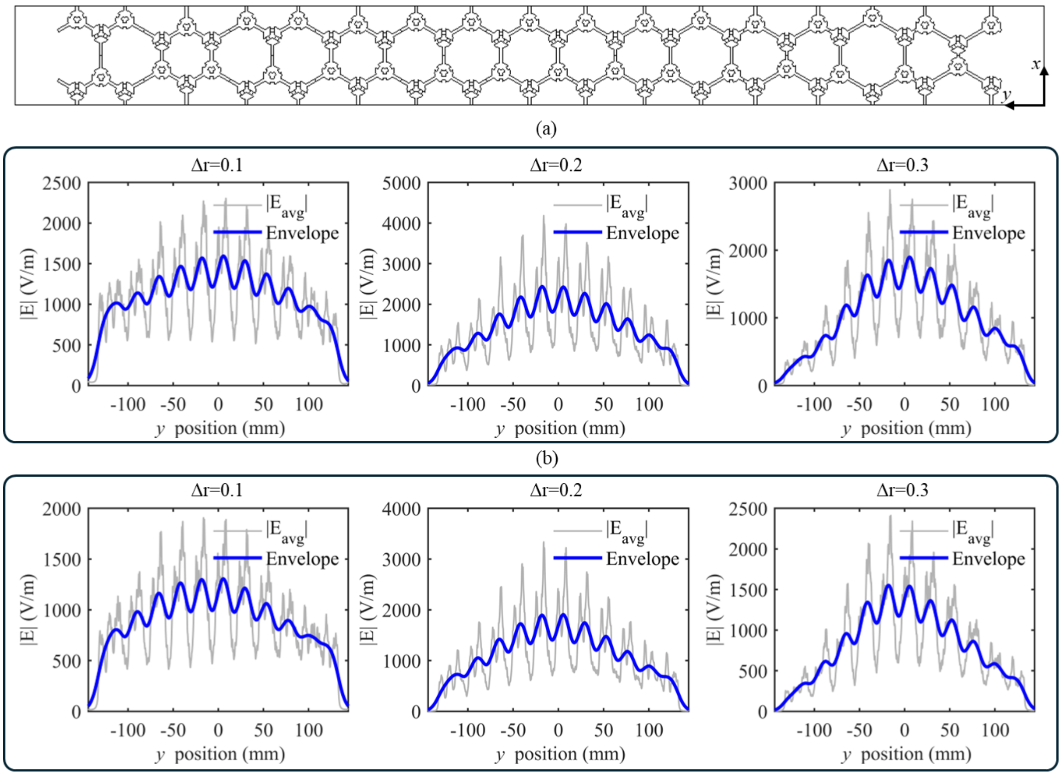

Fig. S11 Electric field profiles of the adiabatic topological edge states. (a) Schematic of the ribbon supercell with a continuous geometric gradient along the transverse direction. **(b, c)** The 1D transverse electric field profiles (grey lines) and their extracted envelopes (blue solid lines) for the two non-Hermitian topological edge modes (Mode 1 and Mode 2) under different geometric gradients (Δr = 0.1, 0.2, and 0.3 mm).

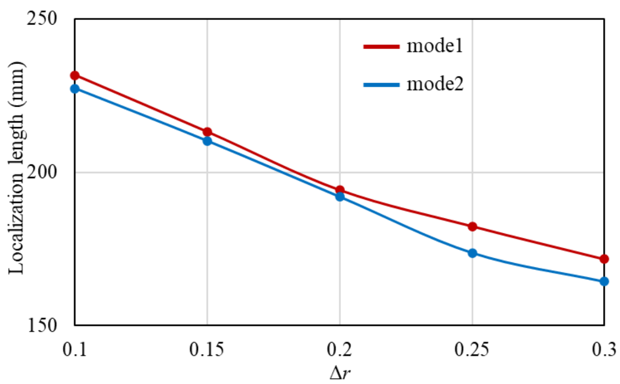

Fig. S12 Quantitative evaluation of the edge state localization length. The calculated localization lengths for both topological modes (Mode 1 and Mode 2) as a function of the geometric gradient Δr. The graph explicitly demonstrates a monotonic decrease, confirming that a steeper spatial gradient tightens the transverse confinement of the adiabatic topological edge states.

S7. Robustness Analysis under Random Manufacturing Tolerances

In practical microwave implementations, lumped resistors exhibit manufacturing tolerances (typically ±10%), which introduce spatial random disorder into the non-Hermitian metasurface. To evaluate the robustness of our complex band topology against such practical imperfections, we performed a statistical Monte Carlo analysis based on the Tight-Binding (TB) Hamiltonian. In each of the 100 random realizations, we introduced uniformly distributed random imaginary on-site potentials $\delta\gamma \in$ [-10%, +10%] independently to all lossy nodes.

Figure S13 presents the Monte Carlo calculations for the unit cell. The gray scatter points represent the superposition of 100 random runs, while the colored solid lines and red dots indicate the ideal scenario without tolerances. Despite the random scattering, the real-part degenerate surface at the Γ point and the macroscopic symmetry-breaking bifurcation in the imaginary spectrum remain highly stable and distinct.

Figure S14 extends this statistical analysis to the inhomogeneous topological supercell. In the complex spectrum plane, the randomly scattered bulk states broaden into a thick horizontal cloud near the average loss level. The topological domain-wall modes located near the real-part degenerate center remain isolated. They largely maintain their differential attenuation characteristics and do not merge into the bulk. This explicit separation confirms that the topological domain-wall modes exhibit robustness to typical manufacturing tolerances.

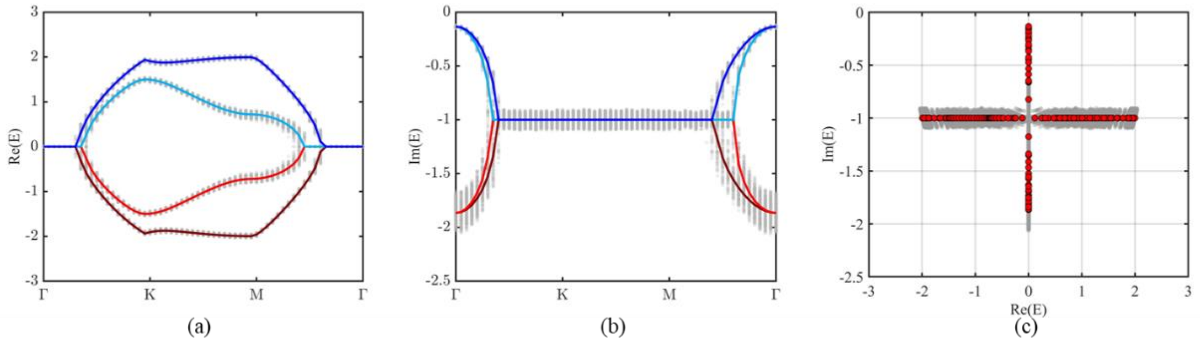

Fig. S13 Monte Carlo robustness analysis under 10% random resistance disorder. (a) The real part of the band structure, (b) the imaginary part of the band structure, and (c) the complex spectrum (Re vs. Im) of the unit cell over 100 random disorder realizations. The gray clouds indicate the tolerance-induced scattering, while the fundamental non-Hermitian bifurcation remains distinguishable.

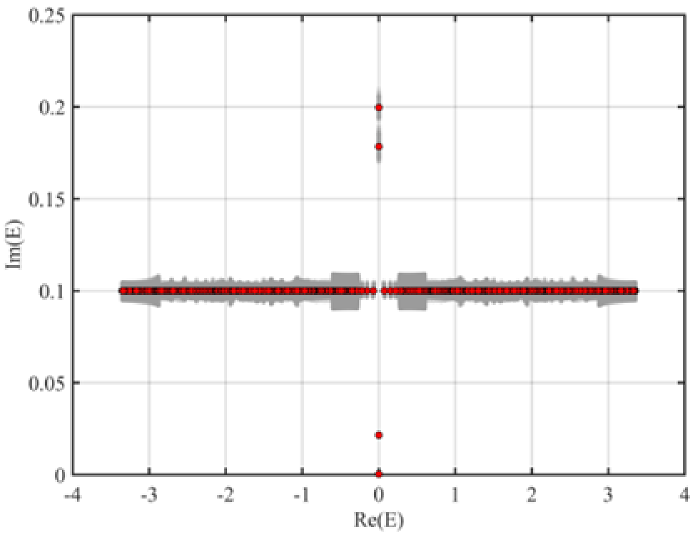

Fig. S14 The complex spectrum of the topological ribbon (supercell) under identical random disorder conditions. The topological edge states (isolated red dots at Re(E)=0) remain inside the complex bandgap and are separated from the broadened bulk-state cloud.

S8. Dispersion Extracted from Full-Wave Simulations via 1D FFT

Figures S15(a) and (c) show the up- and down-going edge states extracted from full-wave simulations of the non-Hermitian inhomogeneous lattice. Their dispersions agree well with the results from the eigenmode solver. Figures S15(b) and (d) display the corresponding electric-field distributions, showing rapid decay due to loss.

Figures S16(a) and (c) present the up- and down-going edge states of the Hermitian inhomogeneous lattice. The dispersions again match the eigenmode analysis, and the field distributions in Figs. S16(b) and (d) confirm efficient propagation under lossless conditions.

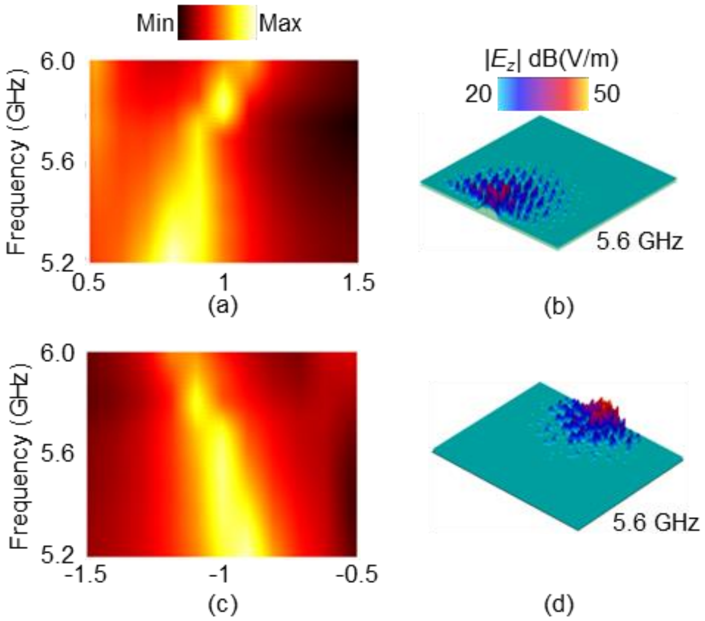

Fig. S15 (a) Up-going edge states extracted from the non-Hermitian model. (b) Field distribution of the up-going states. (c) Down-going edge states extracted from the non-Hermitian model. (d) Field distribution of the down-going states.

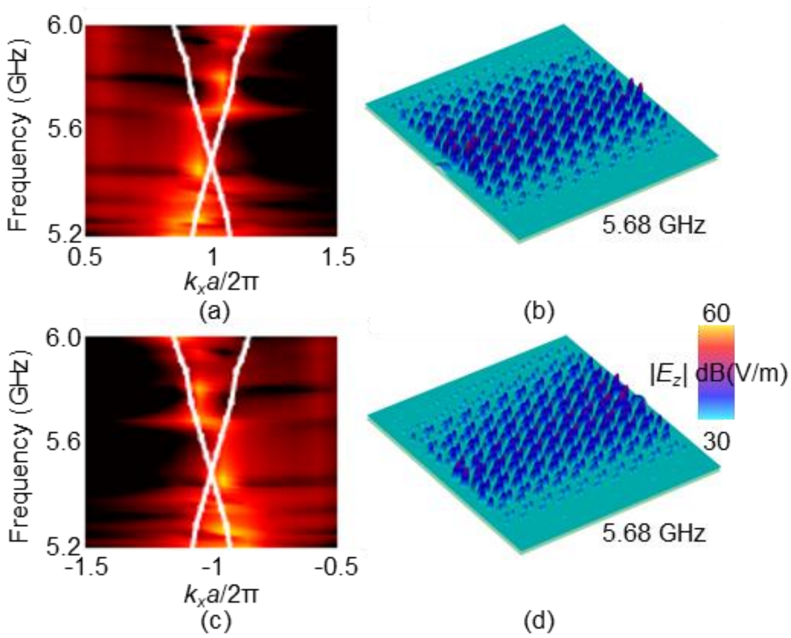

Fig. S16 (a) Up-going edge states extracted from the Hermitian model. (b) Field distribution of the up-going states. (c) Down-going edge states extracted from the Hermitian model. (d) Field distribution of the down-going states.

S9. Defect Scattering Comparison between Hermitian and Non-Hermitian Edge States

To quantitatively evaluate the influence of local defects on the edge-channel propagation, we performed full-wave simulations for both the Hermitian and non-Hermitian inhomogeneous lattices. The Hermitian counterpart was obtained by replacing the resistive elements with lossless metallic connections, while the same spatially graded lattice geometry was retained. A local obstacle was introduced by removing one unit cell near the domain wall. The same excitation condition was used for the Hermitian and non-Hermitian systems.

Figure S17 compares the simulated field distributions and transverse field profiles. In the clean systems, the edge-channel propagation is guided by the domain wall. After the obstacle is introduced, both the Hermitian and non-Hermitian systems still support edge-channel propagation, indicating that the local defect does not destroy the topological interface. However, the Hermitian system shows more pronounced field spreading away from the interface immediately after the defect, while the non-Hermitian system maintains a relatively more compact field distribution around the domain wall.

To quantify the defect-induced bulk leakage, we extracted the transverse field profile after the obstacle by averaging the electric-field amplitude over one lattice period along the x-direction:

$$\left\langle \left|E_z\right| \right\rangle_x (y) = \frac{1}{p}\int_{x_0}^{x_0+p} \left|E_z(x,y)\right| dx \tag{S11}$$

where p is the lattice period along the propagation direction. The normalized transverse profiles show that the non-Hermitian system suppresses several off-interface side lobes that appear in the Hermitian counterpart.

For a more quantitative comparison, we calculated the bulk-leakage ratio using the x-averaged field intensity:

$$\eta_{bulk} = \frac{\int_{\text{bulk}} \left\langle \left|E_z(x,y)\right|^2 \right\rangle_x d_y}{\int_{\text{all}} \left\langle \left|E_z(x,y)\right|^2 \right\rangle_x d_y} \tag{S12}$$

Here, the bulk region is defined as the region outside the edge-channel window. To confirm that the conclusion is not sensitive to the selected window size, three criteria were tested: $|y|>40$ mm, $|y|>50$ mm, and $|y|>60$ mm. In the first few periods after the obstacle, the non-Hermitian system exhibits a lower bulk-leakage ratio than the Hermitian counterpart. This indicates that the engineered loss suppresses the bulk-like scattered components generated by the defect. At longer distances from the obstacle, the leakage ratios become comparable because the remaining field is redistributed along the edge channel.

These results indicate that the role of non-Hermiticity is not simply to attenuate the total field amplitude. Instead, the engineered loss provides a dissipation-assisted modal-filtering mechanism, reducing defect-induced bulk leakage and improving the modal purity of the edge-state response.

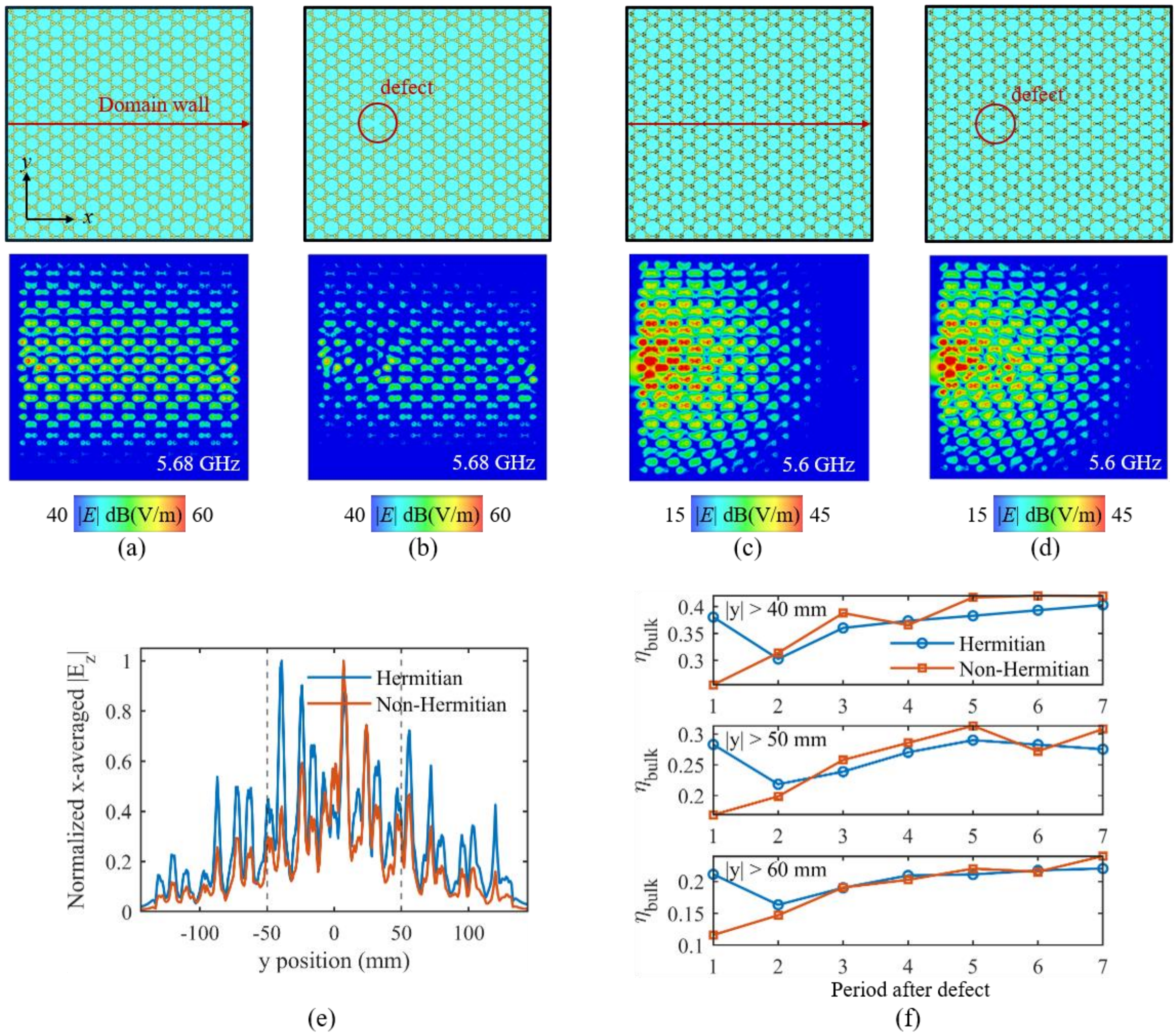

Fig. S17 Defect scattering comparison between Hermitian and non-Hermitian edge states. (a,b) Schematic illustrations and simulated field distributions of the Hermitian inhomogeneous lattice without and with a local defect. The defect is introduced by removing one unit cell near the domain wall. (c,d) Corresponding schematic illustrations and simulated field distributions of the non-Hermitian inhomogeneous lattice without and with the same local defect. (e) Normalized transverse field profiles extracted from the first lattice period after the obstacle. The profiles are obtained by averaging $|E_z(x,y)|$ over one period along the x-direction and normalizing each curve by its maximum value. The dashed lines indicate the selected edge-channel window. (f) Bulk-leakage ratio η_{bulk} as a function of the lattice period after the obstacle. Three different definitions of the bulk region, $|y|$>40 mm, $|y|$>50 mm, and $|y|$>60 mm, are used to test the robustness of the conclusion.

S10. Chiral Excitation Source and Synthetic Coherent Multi-Probe Measurement

To accurately simulate the chiral excitation of the pseudospin-dependent edge states, a circularly polarized source was constructed at the center of the topological domain wall, as shown in Figure S18. The source consists of an array of six discrete ports (labeled P1 to P6) connecting to the metallic disks of the central unit cell.

The chiral excitation is generated by feeding these six ports with equal signal amplitudes while maintaining a constant phase difference of 60° between adjacent ports. This synchronized 6-port configuration effectively creates a rotating phase profile that selectively couples to the topological pseudospin, enabling the unidirectional transport demonstrated in the main text.

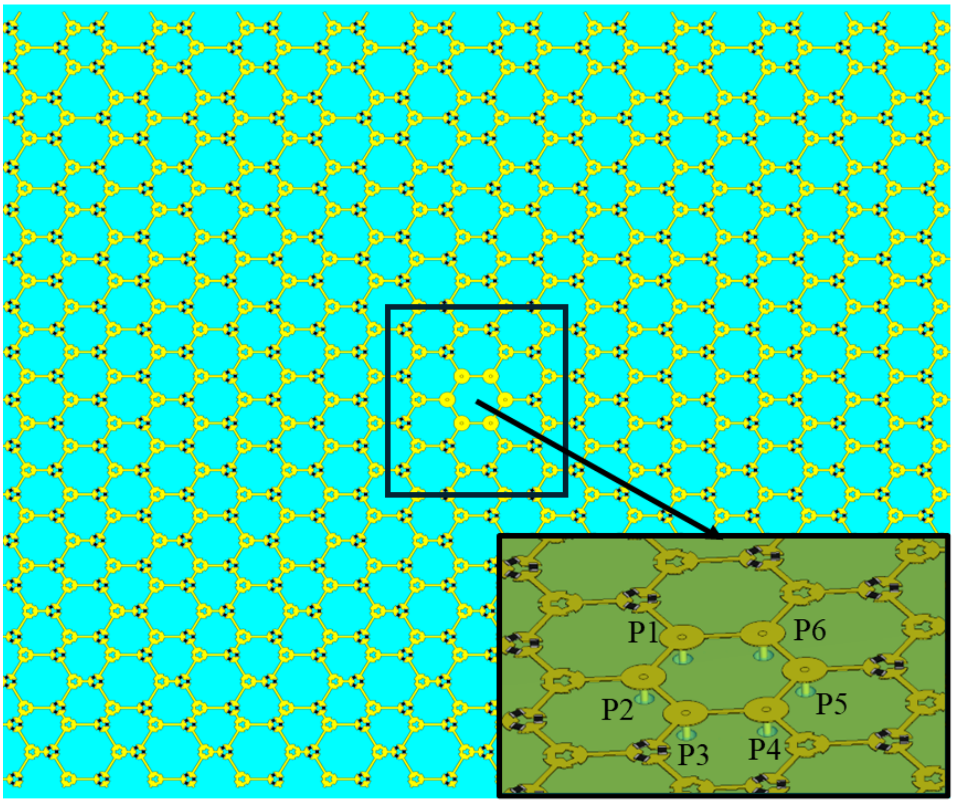

Fig. S18 Simulation setup for the chiral excitation source. The black solid box indicates the central unit cell located at the topological domain wall. The inset shows an enlarged view of the excitation array, which comprises six discrete ports (P1–P6) arranged hexagonally to mimic a true circularly polarized source via equal amplitudes and a 60° phase difference between adjacent ports.

To further verify the chiral excitation experimentally, we performed a synthetic coherent multi-probe measurement. As shown in Fig. S19(a), three excitation probes, denoted as P1, P2, and P3, were soldered near the central region of the domain-wall interface. Two additional probes were soldered at the left and right sides of the interface and served as receiving ports.

During the measurement, the three excitation probes were driven sequentially. When one excitation probe was connected to the vector network analyzer, the other two excitation probes were terminated with matched loads. This configuration ensures that the boundary condition of the multi-probe system remains consistent during the sequential measurements. The complex transmission responses from each excitation probe to the left and right receiving ports were recorded as $S_{L,n}$ and $S_{R,n}$, where n = 1, 2, 3 labels the excitation probe.

Because the microwave system operates in the linear regime, the response to an arbitrary coherent three-probe excitation can be reconstructed by linearly superposing the individually measured complex responses. For a chiral excitation with equal amplitudes and a 120° phase difference, the excitation coefficients are chosen as:

$$a_1 = 1, a_2 = e^{i2\pi/3}, a_3 = e^{i4\pi/3} \tag{S13}$$

The synthesized complex transmission responses are then calculated as:

$$S_{L,syn} = a_1 S_{L,1} + a_2 S_{L,2} + a_3 S_{L,3} \tag{S14}$$

$$S_{R,syn} = a_1 S_{R,1} + a_2 S_{R,2} + a_3 S_{R,3} \tag{S15}$$

The normalized transmission coefficients are obtained from $S_{L,\mathrm{syn}}$ and $S_{R,\mathrm{syn}}$ after normalization. As shown in Fig. S19(b), the synthesized right-side transmission is stronger than the left-side transmission within the operating frequency range. This result provides experimental support for the conclusion that the synthesized chiral excitation preferentially couples to the right-propagating topological edge mode, consistent with the simulated pseudospin-momentum-locked excitation behavior.

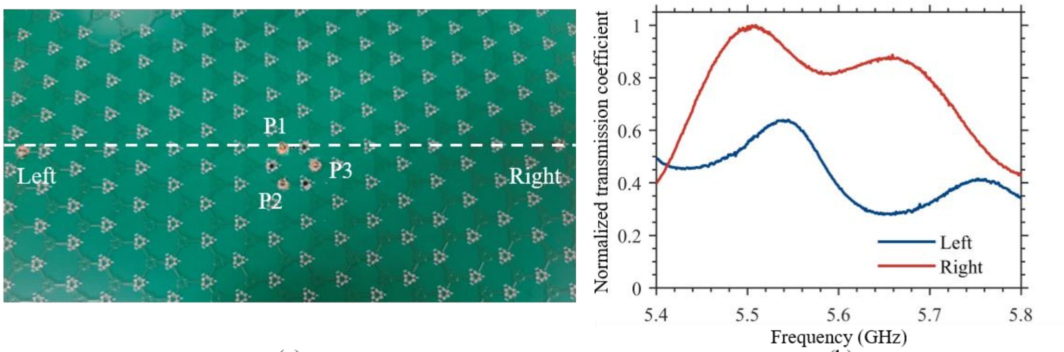

(a) (b)

Fig. S19 Experimental verification of synthetic chiral excitation. (a) Photograph of the microwave sample. Three excitation probes P1–P3 are soldered near the central region of the domain-wall interface, while the left and right receiving probes are placed at the two sides of the interface. During the sequential measurements, one excitation probe is driven at a time and the remaining excitation probes are terminated with matched loads. (b) Synthesized normalized transmission coefficients to the left and right receiving ports. The three measured complex responses are coherently combined with equal amplitudes and a 120° phase difference. The stronger right-side transmission supports the preferential excitation of the right-propagating edge mode.